7th International Conference on Crack Paths

Fatigue fracture surface investigations with a 3D optical profiler

C. Santus[a]*, P. Neri[a], L. Romoli[b], A. Lutey[b], S. Raghavendra[c], M. Benedetti[c]

University of Pisa, DICI – Largo Lucio Lazzarino, 1 – 56122 – Pisa, Italy
University of Parma, DIA – Parco Area delle Scienze, 181/A – 43124 – Parma, Italy
University of Trento, DII – Via Sommarive, 9 – 38123 – Povo (TN), Italy

Abstract

In this paper a set of specimens, used for the critical distance determination, are investigated with a non-contact 3D optical profiler. The fatigue fracture surfaces of both plain and V-notched specimens, under axial (mode I) and torsional (mode III) loadings are observed, investigating steel 42CrMo4+QT and aluminium alloy 7075-T6. The fatigue fracture profiles are compared to be previously obtained critical distances, both for mode I and mode III. The stage I to stage II transition was found at a smaller size than the axial critical distance, for the steel, while for the torsional load a local plateau at the nucleation was observed. The fracture surface of the axial loading was instead much irregular at the scale of the mode I critical distance, for the aluminium alloy, resembling a not concluded stage I, while again a relatively flat surface was observed for the mode III loading.

1. Introduction

The recent research on the fatigue strength of materials focuses on the definition of a material length which can be considered the size of a process volume, where the stress and strains according to different criteria need to be averaged instead of just considering the maximum values at the notch tip. According to the Theory of Critical Distances (TCD), this length is a material property, however, it also depends on the load ratio, and most importantly on the load type. For these reasons, an accurate and reliable determination of the critical distance is recommended for an effective

* Corresponding author. Tel.: +39-(0)50-2218007.
  E-mail address: ciro.santus@unipi.it

implementation of any fatigue criterion. In principle, this length should be obtained from the threshold stress intensity factor range and the unnotched, or plain specimen, fatigue limit. Nevertheless, the threshold is not easy to be determined and it can be subjected to the effect of how the specimen was precracked. Therefore, the critical distance is usually determined by combining the fatigue strength of the plain specimen and that of a notched specimen, especially by selecting a sharply notched specimen for a more reliable identification of the critical distance value. Santus et al. (2018) proposed a procedure to implement this approach. An optimized V-notched specimen was defined, and an inverse search numerical function was proposed for a fast and accurate calculation. Santus et al. (2018-ii) then proposed an experimental activity on two common high strength metals: the steel 42CrMo4+QT and the aluminium alloy 7075-T6, and providing successful comparisons with the critical distances obtained from the thresholds of the two materials. Benedetti and Santus (2020) then provided the statistic evaluation of the critical distance, as a result of the uncertainty of the plain and notched fatigue strengths, and obtained a skew-normal distribution of the critical distance. Santus et al. (2021) subsequently extended the entire approach to the mode III loading, and after considering the fatigue data of the same materials, significantly larger torsional (or mode III) critical distances were obtained with respect to the (common) mode I, or axial, critical distance.

The specimens used for these critical distance determinations are investigated in the present work, by performing high resolution, three-dimensional, acquisitions and reconstruction of the fatigue fracture surfaces. An optical 3D profiler was used in this activity instead of the more common SEM technology, basically for practical reasons: the acquisition is faster and, most importantly, the entire matrix of the acquisition points can be extracted and then elaborated, instead of bidimensional (and static) images. And this allows the full understanding of the fracture surface morphology. In principle this technology is devoted to the investigation of the machined surfaces, just to improve the limitations of the traditional contact profilers. However, there are several examples of different applications of this facility, such as to determine the texture of stainless steel surfaces in the food industry, Lazzini et al. 2017. Another interesting application was recently proposed by Nicoletto et al. 2019 and Uriati et al. 2021, showing additively manufactured (as-built) surfaces and then correlating the obtained surface properties to the fatigue performances.

2. Non-contact 3D optical profiler

The optical profiler used in this work employs the coherence correlation interferometry (CCI) and as mentioned in the Introduction, was used here to acquire the topography of fatigue fracture surfaces. In CCI a light source is divided into two paths where one travels to a precision reference surface located within the objective and the other travels to the test surface. The reflections from these two surfaces combine at a camera detector where they produce an interference fringe representing the surface topography.
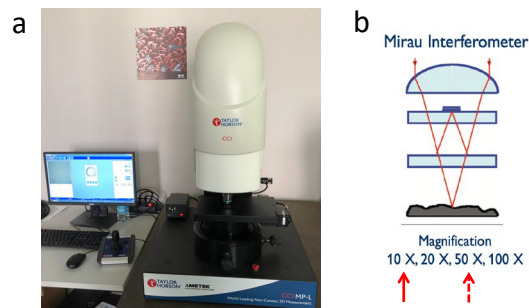

Fig. 1. (a) Taylor Hobson CCI MP-L Optical Profiler; (b) Working principle of the Mirau interferometer.

Acquisitions are performed at regular intervals on the plane perpendicular to the vertical direction and are combined with software to produce the final measurement. The instrument utilized for these analyses, Fig. 1, was equipped with both 10× and 50× objectives with the characteristics shown in Table 1, and with a vertical resolution of less than 1

nm. The 10× objective was employed for most of the measurements, due to the higher field of view, which allowed a larger portion of the surface to be acquired.

Table 1. Optical Profiler parameters and objective properties.

Objective	Field of view (mm)	Pixel size (µm)	Max. slope (°)	Working dist. (mm)	Max. vertical span (µm)	Design
10×	1.73 × 1.73	1.63	8.6	7.4	500	Mirau
50×	0.346 × 0.346	0.329	27.5	3.4	500	Mirau

An example of application of this profilometer is reported on Fig. 2. The specimen in this preliminarily test was plain and the load axial fatigue. As a validation of the surface acquisition, both broken parts of the specimens were relieved, at the fracture surfaces, and then acquired and compared in a CAD environment. The two surfaces resulted quite conformal, as evident in the figure, so not only validating the acquisition instrumentation and software, but also confirming that any damage to the fracture surfaces was introduced.
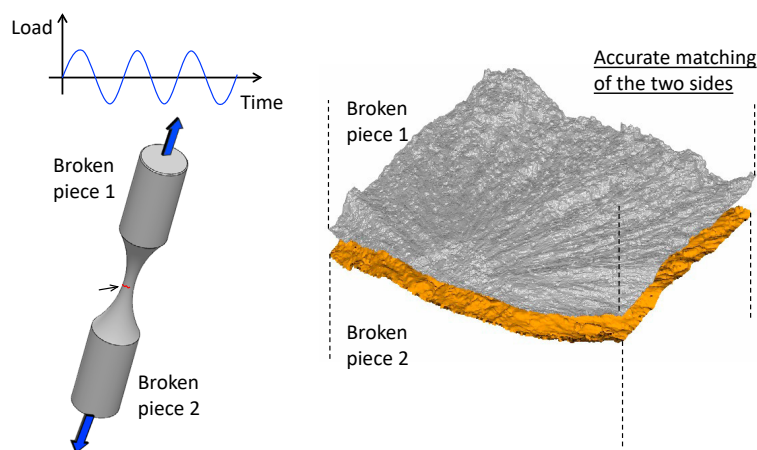

Fig. 2. Application of the profilometer to fatigue fracture, example of matching between the two observed sides of a fatigue fracture surface.

3. Investigated specimens

In order to avoid, or at least limit, any material non-uniformity, specimens were derived from bars of the same production batches, for both the investigated metal alloys, Fig. 3 (a). The axial load induces a high gradient stress at the vicinity of the notch root, according to the linear elastic material model. The notch-stress intensity factor (N-SIF) would imply a singular stress, which however is eliminated when a local radius is measured, thus the actual gradient at that region is strongly dependent on the notch radius itself, Fig. 3 (b). The critical distance L is therefore expected to fall inside of this region, and then it can be deduced according to the either the Line or the Point Method. A similar scheme can be also followed for the fatigue mode III loading, Fig. 3 (c). The stress component is a shear and again the singularity would be expected for a perfectly sharp notch, while a finite value at the root is obtained, still preserving a high gradient. A mode III, or torsional, critical distance L_T can be defined again considering Line or Point Methods.

After the availability of the fatigue strengths of the two plain and notched specimens, for both types of loadings, their ratio (viz. the fatigue stress concentration factor K_f) can be easily calculated, and this is the experimental input of the numerical procedure which leads to the determination of the critical distances L and L_T. In principle, any notch could be used in combination of the plain specimen for the determination of the critical distance. However, a notch as sharp as possible is strongly recommended for having a reliable inverse search. As schematically reported in Fig. 4 (a), if the plain specimen is combined with a blunt notch, showing a local radius in the order of 1 mm, any experimental bias introduces a large effect in terms of the deduced length, being the local gradient not very large, Fig. 4 (b).
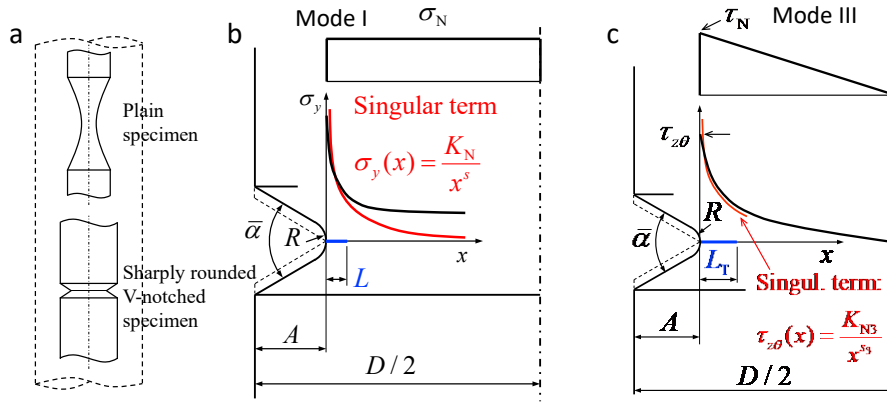
Fig. 3. (a) Plain and V-notched specimens extracted from bars. Stress distributions of the V-notched specimen under mode I (b) and mode III (c), and fatigue critical distances under mode I and mode III inside the high gradient stresses.

For this reason, a very sharp (or ultra-sharp) notched specimen is recommended, and moreover a detection of the actual notch radius is recommended for an effective application of the procedure. This local radius should in principle be equal to the turning tool tip, after imposing a not-radiused V-path. However, the exact size of the resulting radius was measured and resulted not strictly equal to the nominal value, as shown in Fig. 4 (c).
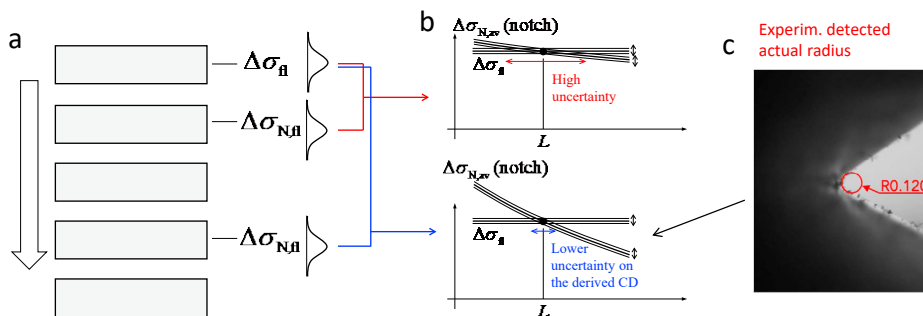

Fig. 4. (a) Different notch severities of specimens for the critical distance determination. (b) More reliable inverse search by combining the plain and a very sharply notched specimen. (c) Detection of the actual notch radius of a ultra-sharp specimen obtained after machining.

Four fatigue test series, for each of the two materials, are reported in Figs. 5 and 6, steel and aluminium alloy respectively. The plain and the V-notched specimens were tested according to both axial loading (mode I) and torsional loading (mode III). The mode I and mode III fatigue limits (plain specimens) are listed in Table 2. After combining these results with those of the V-notched specimens, the proposed inverse search determination procedures were applied and the two critical distances were obtained, for each of the two materials, along with their standard deviations. These results are reported in Table 2.

For each of the experimental series, a single specimen was extracted and dedicated to the fatigue surface investigation. After the verification reported in Fig. 2, just one of the two pieces, of the broken specimen, was put under observation. The selected specimens are highlighted in Figs. 5 and 6 and tests close to the fatigue limits were preferred. The several specimens are referred hereafter to as: P (plain) or N (notched), and I (mode I) or III (mode III).

The specimen fracture surfaces did not require any treatment or cleaning procedure. The observation results are provided in the following sections. Most of the specimens were just put along the vertical direction without any external support. On the contrary, for one specimen under torsional loading, the fracture surface had an inclined layout, thus a support tool with a precise angle was prepared for an optimal observation configuration. As reported in Table

1, the used instrument and the related software, at the present configuration, limited the vertical range, and the maximum span is 500 µm. For this reason, an almost planar target surface, to be observed, is required. However, the availability of the entire set of acquisition points allows a post-processing and then a re-orientation of the acquired surface, just to have the correct alignment of the vertical axis.
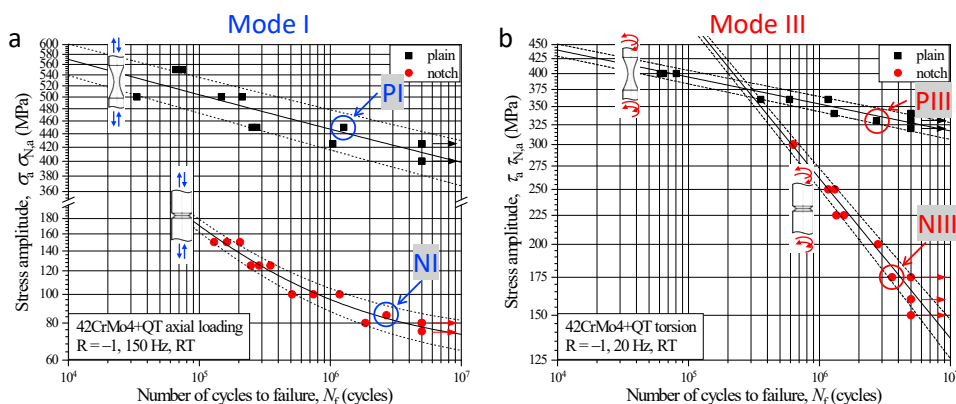

Fig. 5. Fatigue tests of steel 42CrMo4+QT and identification of the investigated specimens, (a) Mode I (or axial) tests on plain and V-notched specimens. (b) Mode III (or torsional) tests on plain and V-notched specimens.
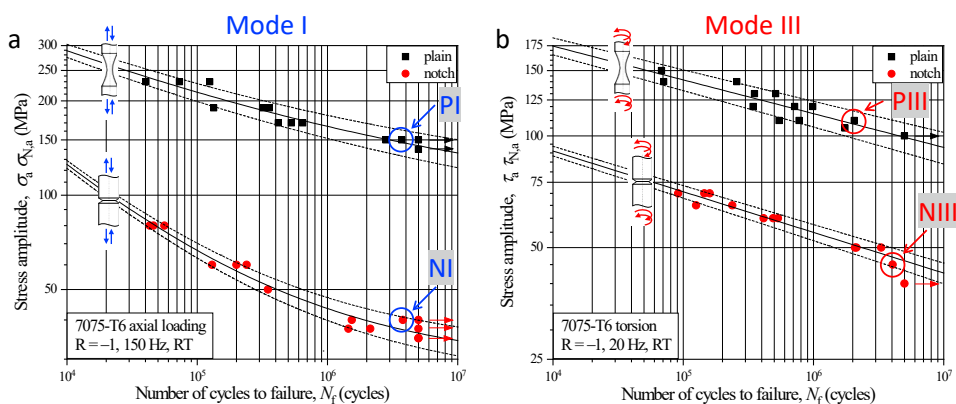

Fig. 6. Fatigue tests of aluminium alloy 7075-T6 and identification of the investigated specimens, (a) Mode I (or axial) tests on plain and V-notched specimens. (b) Mode III (or torsional) tests on plain and V-notched specimens.

Table 2. Mode I and mode III critical distances, obtained with plain and V-notched specimens, for steel and alum. alloy.

Material	Mode I fatigue limit (MPa)	Mode I critical distance (mm)	Mode I cr. dist. stand. dev. (mm)	Mode III fatigue limit (MPa)	Mode III critical distance (mm)	Mode III cr. dist. stand. dev. (mm)
Steel 42CrMo4+QT	412	0.027	0.012	316	0.252	0.043
Alum. alloy 7075-T6	144	0.070	0.022	99	0.201	0.053

3.1. Steel 42CrMo4+QT specimens

In this section the steel specimens are presented. The fatigue fracture of the plain specimen under mode I loading is initially investigated. The specimen was just put under observation without any external support, Fig. 7 (a). The

acquisition obtained with the 10× objective is shown in Fig. 7 (b). The curved (or round) profile of the boundary is at the bottom left side, as evident from the figure. And the faint marks leading to the middle of this boundary suggested the position of the initiation, or nucleation, region.
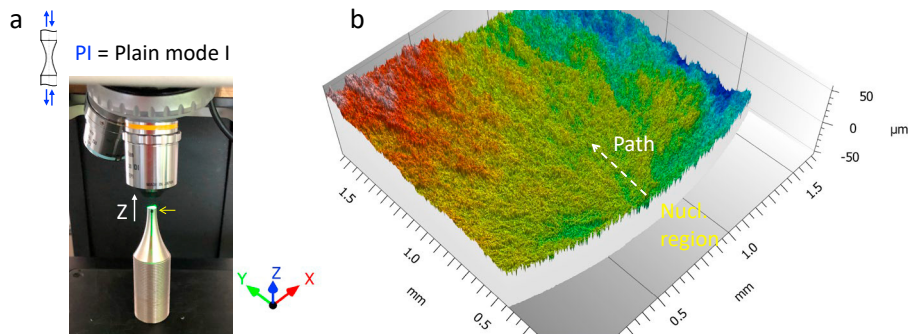

Fig. 7. Steel plain specimen, mode I. (a) Specimen orientation. (b) Profiler observation at the nucleation region.

This fracture surface was also observed with the 50× objective to have a zoomed view of this nucleation region, Fig. 8 (a). In a specific position of this higher resolution observation, it was noticed a small inclined plane at the boundary which can be recognized as the well-known transition from stage I to stage II fatigue initiation. By exploiting the availability of the acquisition points, a bidimensional path was extracted and compared to the size of the (mode I) critical distance. It is evident a quite sudden change of the slope, at the transition, and this happened at a size which resulted approximately 1/3 of the critical distance length.
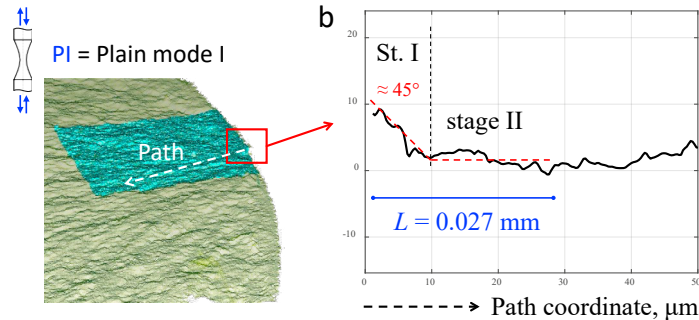

Fig. 8. (a) Superimposition of the 10× and 50× acquisition maps at the nucleation region. Profile extracted from a path starting from the fracture surface boundary, and evidence of the stage I to stage II transition.

The steel V-notched specimen loaded under mode I is presented in Fig. 9, where figure (a) reports the orientation, which is the same as the previous specimen, and figure (b) shows the fracture surface acquisition. As for the plain specimen, the whole surface features a quite planar layout, without any evident irregularity, at least at this observation scale. The boundary at the edge of the notch resulted quite uniform and thus the position of the nucleation did not result evident. A path perpendicular to the boundary was again considered and a bidimensional plot is reported in Fig. 10. Figure (a) shows the overall acquisition, and it is evident the portion of the notch radius. The same profile is observed at a zoomed view in figure (b). The stage I to stage II transition is again evident in this latter view. The stage I portion can be assumed as two inclined segments with angular orientation close to 45°. The mode I propagation starts at a size in the order of 1/2 of the axial critical distance and then remains approximately flat.

The steel plain specimen under torsion reported a more complex surface. A view with a stereo microscope, Fig. 11 (a), allowed the identification of the semi-elliptical nucleation site. Due to not planar layout of the fracture surface at

this nucleation region, the specimen was held with a support providing an inclination of 30°, Fig. 11 (b). The acquired 3D profile, with this preliminarily inclination, is reported in Fig. 11 (c). The measured profile points were then numerically counter-rotated to compensate this initial 30° inclination, thus retrieving the axis of the specimen as vertical Z axis, Fig. 11 (d).
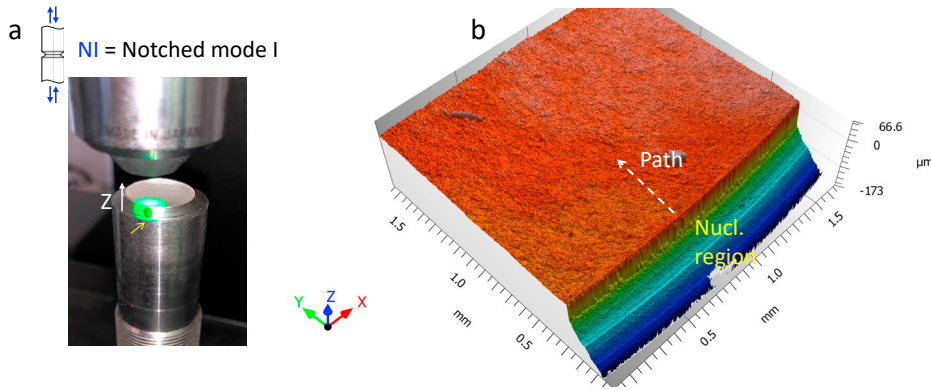

Fig. 9. Steel V-notched specimen, mode I. (a) Specimen orientation. (b) Profiler observation at the nucleation region.
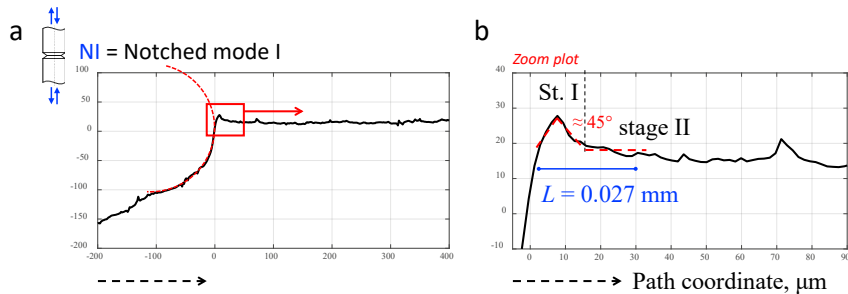

Fig. 10. Steel V-notched specimen, mode I. (a) Bidimensional profile along a path at the fracture surface boundary in the nucleation region. (b) Zoomed view of this profile and comparison of the stage I to stage II transition with the mode I critical distance.

The mode III critical distance of the steel resulted quite larger than the axial counterpart, and it is almost an order of magnitude higher, as reported in Tab. 2. After comparing this large length and the (re-oriented) fracture surface reconstruction, Fig. 11 (d), it can be noted that the plateau observed perpendicular to the specimen axis, is of the same size of the torsional critical distance. In other words, this length is similar to the nucleation ellipse semi-axis, along the direction perpendicular to the surface boundary. After the initial propagation phases, the crack under torsional loading experiences a very complex path, which in principle can be reconstructed with this proposed optical methodology, however, less interesting in terms of fatigue nucleation. Nevertheless, a mode I propagation can be identified in the left upper side of Fig. 11 (d), where the normal stress obviously acts as the driving force. On the contrary, the shear stress can be considered the reference for the nucleation.

Fig. 12 finally reports the acquisition of the fracture surface of the steel V-notched specimen, under mode III fatigue loading. Fig. 12 (a) shows again a stereo microscope image of the nucleation region, while figure (b) shows the optical profiler acquisition with the vertical axis oriented as the specimen axis. Even for this notched specimen, the nucleation region is well distinguished with respect to the irregular surface of the subsequent propagation. The common factory-roof structure was well evident, and large ridges showing 45° inclinations were observed, also extended at the notch boundary. By assuming that the factory-roof formations are generated as a further propagation step, the nucleation still happens on a planar region, and the size of this local plateau is even wider than the (large) fatigue mode III critical distance. In agreement with the previous specimen (plain and mode III), despite the evidence of further inclined

propagations, the fatigue crack nucleation can be again attributed to a shear mechanism, after assuming that the critical plane is consistent with the orientation of the crack evidence.
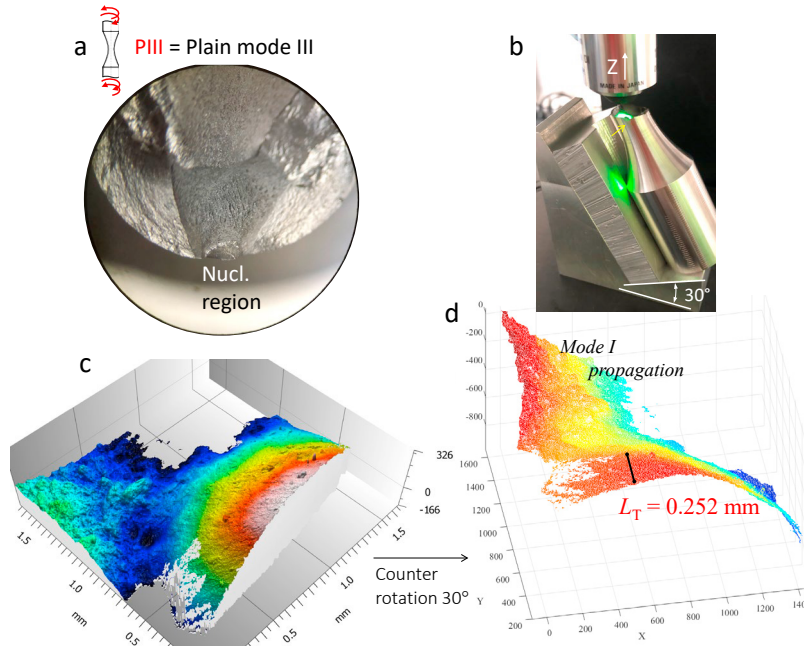

Fig. 11. Steel plain specimen, mode III. (a) stereo microscope view of the nucleation region. (b) Specimen inclined setup for the optical profiler. (c) Observation obtained at the nucleation region. (d) Re-orientation of the acquisition map and comparison between the nucleation region and the fatigue mode III critical distance.
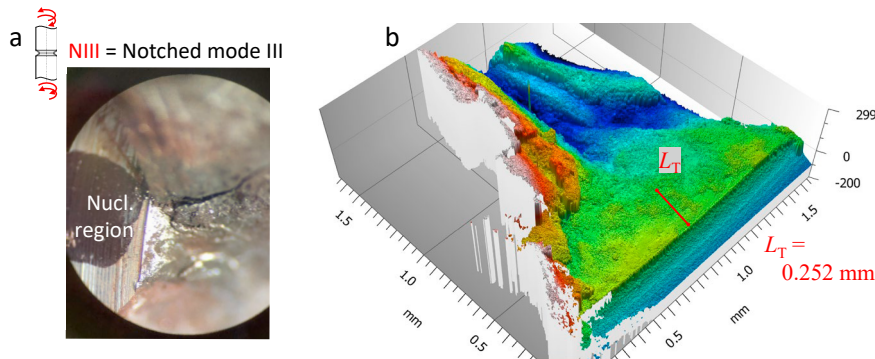

Fig. 12. Steel V-notched specimen, mode III. (a) Stereo microscope observation at the nucleation region and evidence of large factory-roof ridges. (b) Profiler observation at the nucleation region and comparison with the fatigue mode III critical distance.

3.2. Aluminium alloy 7075-T6 specimens

The same specimen sequence was repeated for the aluminium alloy, and similar results were obtained, however, with an evident more irregularity of the observed surfaces. Fig. 13 (a) and (b) show the profiler acquisitions of the plain and notched specimens, respectively, fractured under fatigue mode I loading. The exact initiation positions were not evident, however, the direction of faint striations again suggested the nucleation regions, which resulted at the right edges of the two acquisitions reported in Fig. 13. Bidimensional path profiles were extracted at these two positions, for both specimens, and reported in Fig. 14. The initial profile along the path starting from the surface boundary of the

plain specimen, Fig. 14 (a), shows an initial irregularity that can be considered as a large stage I, which overlaps the entire size of the (axial) fatigue critical distance. On the contrary, an almost uniform inclination was observed for the profile of the notched specimen, Fig. 14 (b). Since the initial crack path is not well aligned with the notch root bisector, and considering the path orientation, the nucleation can be attributed to the normal stress, instead of shear, because the observed crack orientation is locally perpendicular to the radiused notch profile.
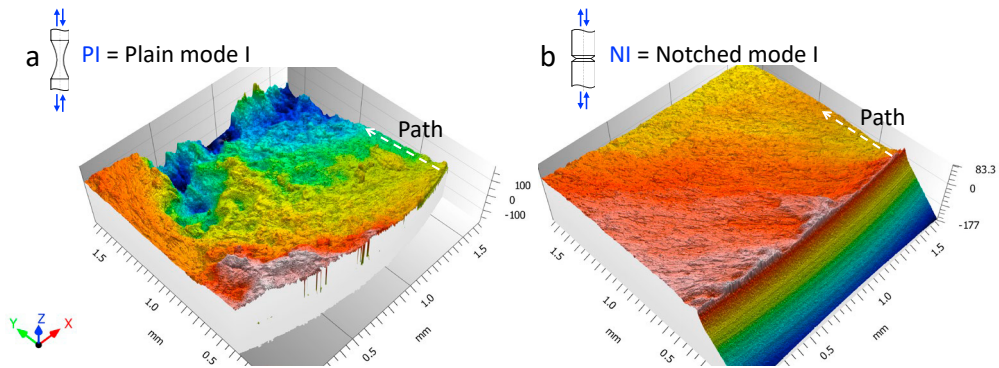

Fig. 13. Aluminium alloy specimens, mode I. (a) Plain specimen and (b) V-notched specimen profiler observations.
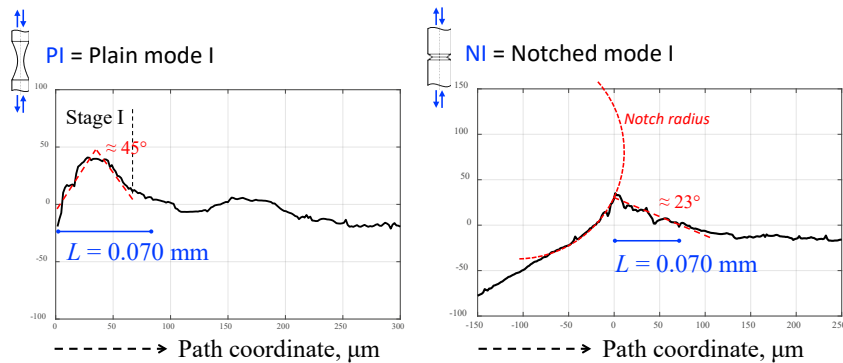

Fig. 14. Aluminium alloy specimens, mode I. (a) Bidimensional profile along a path at the fracture surface boundary, in the nucleation region: (a) plain specimen, (b) V-notched specimen.
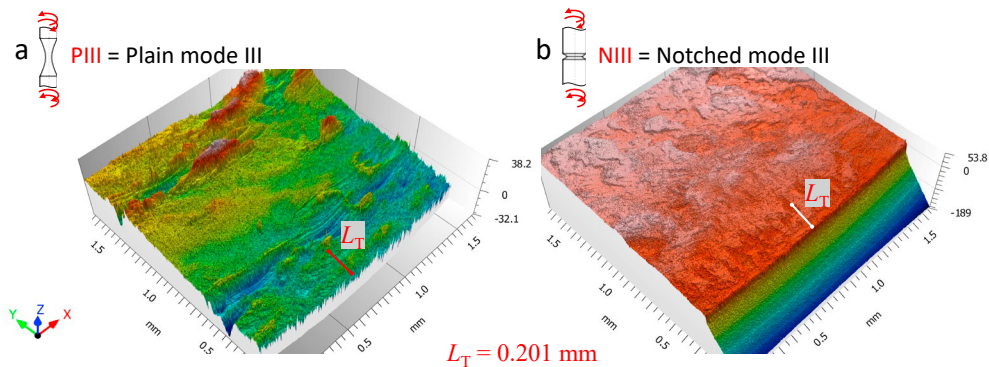

Fig. 15. Aluminium alloy specimens, mode III. (a) Plain specimen and (b) V-notched specimen profiler observations.

The fatigue fracture surface acquisitions of aluminium alloy plain and V-notched specimens, under torsional fatigue, are finally shown in Fig. 15 (a) and (b), respectively. The observed fracture surfaces resulted quite flat and for both specimens the factory-roof formations were not visible. Tangential striations can be observed for the plain specimen only, Fig. 15 (a). Nevertheless, these striations resulted not at the surface boundary. Thus, they cannot be attributed to a nucleation mechanism, since the (mode III) critical distance is assumed as a measure of the nucleation size. Therefore, the mode III can be considered shear driven in similarity with the steel previously observed. The near surface nucleation was in fact along a local plateau on which the shear stress is maximum, and the normal stress is null, for both the plain and the V-notched specimens.

The evidence of more irregular fracture surfaces of the aluminium alloy specimens, with respect to the steel, especially under mode I loading, can be attributed to a larger grain size combined with elongated grains, as deeply investigated by Benedetti et al. 2021. On the contrary, the steel microstructure featured considerable smaller and more regular grains.

4. Conclusions

In this work an optical (contactless) three-dimensional profiler was successfully used for the post fracture investigations of steel 42CrMo4+QT and aluminium alloy 7075-T6 fatigue tests, under both axial (mode I) and torsional (mode III) loadings. Quite easy and relatively quick acquisitions were obtained, the resolution was adequate in-plane and very accurate along the vertical direction. Specific features were observed for the two investigated metal alloys. The steel produced flat mode I and mode III nucleation regions, at least at an observation scale of the size of the critical distances. More irregular fracture surfaces were observed for the aluminium alloy, in particular under mode I loading, while again quite planar surfaces were obtained under torsion.

The detection of the crack orientation, at the initial stages, is considered a valid indicator for the identification of the correct fatigue criterion (either multiaxial or uniaxial) to be considered for the strength assessment. In particular, a normal stress criterion can be suggested for the steel, under mode I loading, while a shear criterion should be considered more effective, under mode III, being the crack planes aligned with the maximum shear stress. A similar conclusion can be repeated for the aluminium alloy under mode III. On the contrary, the mode I crack nucleation featured an inclined and quite irregular morphology, for the plain specimen, thus suggesting a shear based criterion, while the notched surface reported a normal nucleation. However, if the Line Method is considered, the averaging size is $2L$ and then the nucleation region can be again approximated as almost perpendicular to the normal stress. According to this, the first principal stress can be reconsidered as the reference criterion. On the contrary, if the Point Method is used, the reference stress evaluation locaton is at $L/2$, thus within the inclined region, and then a shear based criterion, such as the Fatemi-Socie parameter, should be proposed. However, the critical distance itself should be recalculated according to that criterion.

References

Santus, C., Taylor, D., Benedetti, M., 2018. Determination of the fatigue critical distance according to the Line and the Point Methods with rounded V-notched specimen. International Journal of Fatigue 106, 208.

Santus C., Taylor D., Benedetti, M., 2018. Experimental determination and sensitivity analysis of the fatigue critical distance obtained with rounded V-notched specimens. International Journal of Fatigue 113, 113.

Benedetti M., Santus C., 2020. Statistical properties of threshold and notch derived estimations of the critical distance according to the line method of the theory of critical distances. International Journal of Fatigue 137, 105656.

Santus C., Berto F., Pedranz M., Benedetti, M., 2021. Mode III critical distance determination with optimized V-notched specimen under torsional fatigue and size effects on the inverse search probability distribution. International Journal of Fatigue 151, 106351.

Lazzini, G., Romoli, L., Blunt, L., Gemini, L., 2017. Design and characterization of textured surfaces for applications in the food industry. Surface Topography: Metrology and Properties 5(4), 044005.

Nicoletto, G., Tinelli, G., Lutey, A., Romoli, L., 2019. Influence of as-built surface topography on the fatigue behavior of SLM Inconel 718: Experiments and modelling. 2nd International Conference on Simulation for Additive Manufacturing, Sim-AM 2019 pp. 83-90.

Uriati, F., Nicoletto, G., Lutey, A.H.A., 2021. As-built surface quality and fatigue resistance of Inconel 718 obtained by additive manufacturing. Material Design and Processing Communications 3(4), e228.

Benedetti, M., Menapace, C., Fontanari, V., Santus C., 2021. On the variability in static and cyclic mechanical properties of extruded 7075-T6 aluminum alloy. Fatigue & Fracture of Engineering Materials & Structures 44(11), 2975.